Impact of ruthenium metallic particles on the dissolution of UO2 in nitric acid

Thibault Kaczmarek, Stéphanie Szenknect, Laurent Claparède, Martiane Cabié, X. F Le Goff, Adel Mesbah, Renaud Podor, Nicolas Dacheux

HAL Id: hal-03862238

https://hal.umontpellier.fr/hal-03862238

Submitted on 24 Nov 2022

ARTICLE OPEN

Check for updates

Impact of ruthenium metallic particles on the dissolution of UO₂ in nitric acid

Thibault Kaczmarek[1], Stéphanie Szenknect [1 ✉], Laurent Claparède [1], Martiane Cabié[2], Xavier Le Goff[1], Adel Mesbah [1], Renaud Podor[1] and Nicolas Dacheux [1]

UO₂ pellets incorporating 3 mol.% of Ru was prepared by using a wet chemistry route and then characterised. The speciation, morphology, as well as spatial distribution of Ru in the sintered samples, were determined. The synthesised samples were submitted to dissolution tests in 0.1 M nitric acid at 60 °C and the dissolution of pure UO₂ pellets was also studied with and without the presence of Ru metallic particles in the solution. The evolution of the U, Ru, and nitrous acid concentrations in solution was measured and the residues of dissolution were further characterised. The obtained results unambiguously demonstrated the catalytic activity of Ru-metal particles during UO₂ dissolution in nitric acid provided that a solid/solid interface existed between UO₂ and Ru-metal particles. This positive impact on the dissolution kinetics of UO₂ was supported by redox reactions taking place at both nitric acid solution/Ru-metal particles and at Ru-metal particles/UO₂ interfaces.

INTRODUCTION

Reprocessing of spent nuclear fuels (SNFs) for the recovery of uranium and plutonium is currently achieved in France using the plutonium uranium reduction by extraction (PUREX) process. Although SNF is composed of about 96 wt.% of UO₂, its composition, and microstructure display an extreme complexity due to the presence of more than 30 Fission Products[1]. Fission products found as metallic precipitates are mainly composed of the noble metals Ru, Rh, Pd, Mo, and Tc (ε-phase) and are manifested as white inclusions[2]. Ruthenium in particular has a direct contribution to SNF reprocessing that is typically based on dissolving the irradiated fuels in hot and concentrated nitric acid[3]. Despite a global content of about 0.47 wt.% or 1.1 mol.% for a UOx irradiated at 50 GWd/t_U, Ru isotopes (103 and 106) are responsible for 10% of the β and γ radiations emitted from the radioactive wastes[4]. Furthermore, even if Ru is eliminated from the nitric acid solution of the SNF as insoluble residues, it is also partially dissolved. Ru (IV) species solubilized during the dissolution of SNFs are quickly converted to the more stable trivalent ruthenium nitrosyl ion, $[Ru(NO)]^{3+}$. Depending on various parameters (pH, nitrate and nitrite ions activities, etc.), $[Ru(NO)]^{3+}$ can form various pseudo-octahedral complexes of the formula $[Ru(NO)(NO_3)_x$ $(NO_2)_y(OH)_z(H_2O)_{5-x-y-z}]^{3-x-y-z}$ [4–7]. These species are co-extracted in the organic phase by tri-n-butyl phosphate (TBP). Consequently, secondary solvent extraction cycles, known as scrubbing, are necessary to purify uranium and plutonium flows and to reduce the subsequent degradation of the solvent by the β-γ-radiation associated with ^{106}Ru[6]. Additionally, Ru tetroxide (RuO_4) is a volatile species that forms during the dissolution step in nitric acid and ultimately during the vitrification process. Gaseous RuO_4 species can decompose when contacting cooler stainless steel surfaces causing the accumulation of a RuO_2 deposit and a local increase in the radiation dose of the plant[8,9]. Finally, the solubility of Ru in the molten glass has been shown to be low[10] and the precipitation of polyhedrons or needle-like crystals of RuO_2 can modify the properties of the glass. Therefore, the conditions of

vitrification of high-level wastes have to be optimised to guarantee the durability of the waste matrix. Considering all these detrimental effects, the increase in the Ru content in the SNF with the increase in burnup needs is a future challenge for the management of the PUREX process. At first, the behavior of Ru in the head-end step of this process is a key issue that deserves to be studied.

Ru remains in the metallic residues of dissolution in association with Mo, Rh, Pd, and Tc[1,11–13]. Adachi et al.[12], studied these metallic residues upon dissolution of pressurised water reactor (PWR) UOx fuel specimens with a burnup range of 7–39 GWd t_U⁻¹. The complete dissolution of SNF was achieved in 4 mol L⁻¹ HNO₃ solution at 100 °C for 2 h regardless of the fuel burnup. The authors observed that the number of insoluble residues increased linearly with burnup and the content of noble metallic precipitates exceeded 70 wt.%. The insoluble residues were enriched with Ru (50–60 wt.% of the five metals), whereas Mo, Rh, Pd, and Tc represented 20, 10–15, 10, and 0.5–5 wt.% respectively. This result indicated that Ru and to a lesser extent Rh were the least solubilized metals during the dissolution step. The particle size distribution of the residues was also determined by Adachi et al.[12] and was found to vary with the dissolution time. Particles of an average hydrodynamic diameter of 100 nm were observed in suspension in the stirred dissolution medium after 2.5 h of dissolution. After 3.5 h, only the larger metallic particles remained to show an average size of 10 to 20 μm. From X-rays diffraction (XRD) analysis of the insoluble residues, the authors concluded that the particles were composed of metallic Ru alloy with a hexagonal structure (ε-phase).

This result was also confirmed by MCC-1 tests performed with synthesised metallic particles of Mo, Ru, Rh, Pd, and Re (used as Tc surrogate) by Wronkiewicz et al.[14]. In these experiments, they observed that the release of platinum group metals (PGM: Ru, Rh, and Pd) was not significant compared to Mo and Re. Cui et al.[2] also collected sub-micron particles remaining after the dissolution of a 23 GWd t_U⁻¹ UOx fuel operated in a PWR for 5 years. In order

to preserve the composition of the metallic particles extracted from the SNF, the dissolution protocol was non-oxidative and consisted in contacting fuel fragments with deoxygenated 85% H_3PO_4 solution at 113 °C for 24 h[15]. Cui et al.[2] observed a hexagonal symmetry of the metallic particles collected in the insoluble residues and a small unit-cell similar to that of elementary Ru. Cui et al.[2] also concluded that the composition of insoluble residues did not match the fission yields. Thus, Ru appeared as the main component of the metallic dissolution residues and the major contributor to their β-γ radiation dose.

The dissolution of spent fuel was mainly achieved in order to study the chemistry and the structure of the metallic residues, but the specific impact of their presence on the kinetics of dissolution of UO_2 matrix received less attention. Ikeda et al.[16] showed a significant increase in the dissolution rate of UO_2 powder in concentrated nitric acid (8 mol L^{-1}) at 60 °C and in the presence of PGM metallic particles (0.09 wt.% of each element). More recently, Cordara et al.[17] performed a multiparametric study on the dissolution of standard UO_2 pellets and pellets doped with 3 mol.% of PGM particles (1.1 mol.% Ru; 1.6 mol.% Rh and 0.3 mol.% Pd). The temperature and the nitric acid concentration varied from 22 °C to 60 °C and from 0.1 mol L^{-1} to 4 mol L^{-1}, respectively. In all cases, the presence of PGM particles led to an increase in the initial dissolution rate of UO_2. This impact was more pronounced at low acidity (typically for HNO_3 concentrations below 1 mol L^{-1}) with a strong decrease in the duration of the induction period. This initial kinetic regime during which the dissolution rate was low, was usually associated with the non-catalysed dissolution reaction (1)[18,19]:

$$UO_2(s) + 2NO_3^-(aq) + 4H^+ \rightarrow UO_2^{2+}(aq) + 2NO_2(aq) + 2H_2O$$

(1)
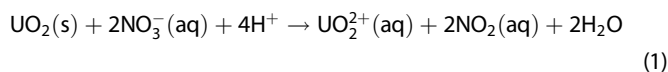
This reaction was slow, but it produced nitrogen species more oxidising than nitrates with respect to UO_2 leading to a strong acceleration of dissolution in the next kinetic step. The presence of PGM particles not only reduced the duration of the induction period, but also drastically changed the apparent activation energy of the dissolution reaction (from 87 ± 8 kJ mol^{-1} to 35 ± 12 kJ mol^{-1})[17]. This result traduced the change of the UO_2 dissolution mechanism caused by the presence of the PGM particles. With the help of environmental scanning electron microscopy (ESEM) monitoring of the solid/solution interface, Cordara et al.[20] also showed that a preferential dissolution of the UO_2 pellet took place in the vicinity of the PGM particles, suggesting that the direct contact between the two solid phases favoured the development of the observed catalytic effect.

Even if all the results obtained previously indicated that the presence of PGM particles promoted the dissolution of the UO_2 matrix in reprocessing conditions, several questions remained unanswered. Firstly, among the PGM elements, the specific role of Ru was not fully elucidated. Secondly, based on the analysis of the standard reduction potentials (calculated versus the normal hydrogen electrode, NHE)[21,22], the kinetic effect of PGM particles remained hypothetical with the reduction of nitrate ions by the metals. Indeed, even if the metallic particles cannot directly oxidise tetravalent uranium to UO_2^{2+} ($E°(UO_2^{2+}/UO_{2(s)}) = 0.294$ V$_{/NHE}$, $E°(UO_2^{2+}/U^{4+}) = 0.327$ V$_{/NHE}$ $E°(Ru^{2+}/Ru) = 0.455$ V$_{/NHE}$, $E°(Rh^+/Rh) = 0.600$ V$_{/NHE}$, $E°(Rh^{3+}/Rh) = 0.758$ V$_{/NHE}$ and $E°(Pd^{2+}/Pd) = 0.951$ V$_{/NHE}$), all of these redox couples (except Pd^{2+}/Pd and Ru^{3+}/Ru^{2+} ($E° = 0.249$ V$_{/NHE}$) are able to reduce nitrate ions into HNO_2 in nitric acid solutions ($E°(NO_3^-/HNO_2) = 0.934$ V$_{/NHE}$). In addition, Kim et al.[23] showed that not only tetravalent Ru could oxidise UO_2, but also Ru (III) could reduce NO_3^- to HNO_2 and was oxidised to Ru (IV). Thus, if the dissolution of Ru metal occurred in nitric acid solution and led to the formation of Ru (III) species, the redox reaction with nitrate ions might produce two oxidants regarding UO_2: HNO_2 and Ru (IV). Nevertheless, all these redox

reactions, which could explain the positive impact of PGM on the kinetics of dissolution of UO_2 involve the dissolution of PGM particles and the production of HNO_2. Unfortunately, in the previous studies reported by Cordara et al.[17], the evolution of the elemental concentration of Ru, Rh, Pd, and HNO_2 in solution was not monitored due to analytical issues.

In order to elucidate the mechanism associated with the presence of PGM particles, we focused in this work on the specific role of Ru as a major component of the five metallic particles inflicting challenges to the PUREX process. For this purpose, we synthesised model samples of pure UO_2, UO_2 doped with 3 mol.% of ruthenium as well as Ru metallic particles. These particles were then introduced in suspension during UO_2 dissolution experiments. The dissolution experiments were performed in 0.1 mol L^{-1} HNO_3 at 60 °C, which corresponded to the conditions of the strong impact of Ru particles according to Cordara et al.[17]. The monitoring of the U, Ru, and HNO_2 concentrations in solution were systematically achieved during the dissolution of the model compounds in nitric acid solution. Additionally, experiments were conducted in 0.1 mol L^{-1} HCl solution in order to compare with the UO_2 dissolution rates determined in nitric acid solution with or without Ru particles.

RESULTS

Characterisations of pristine samples

The UO_2, UO_2/Ru, and Ru^0 powders synthesised by the hydroxide precipitation method were characterised by powder X-ray diffraction (PXRD) (Supplementary Fig. 1). The XRD patterns of uranium-containing samples showed the XRD lines related to the fluorite structure characteristic of UO_2 (space group $Fm\overline{3}m$). The pattern of Ru^0 particles showed the XRD lines related to the hexagonal structure of space group $P6_3/mmc$. The associated unit-cell parameters obtained by Rietveld refinement of $a = 2.7051(1)$ Å and $c = 4.2825(1)$ Å were in agreement with those determined by Wronckiewicz et al.[14] for the five-metal particles ($a = 2.710$ Å and $c = 4.280$ Å). The PXRD pattern of the UO_2 sample doped with ruthenium showed the XRD lines characteristic of the fluorite-type structure (with $a = 5.4538(2)$ Å, Supplementary Fig. 2) and additional XRD lines caused by the sample holder. The unit-cell parameter of the fluorite-type structure phase in the UO_2/Ru sample was smaller than that in stoichiometric UO_2 ($a = 5.47127(8)$ Å) as measured by Leinders et al.[24]. This result suggested that Ru was not incorporated in the UO_2 structure, but presented as a minority and unknown phase in the prepared powder prior to sintering.

SEM micrographs of UO_2, UO_2/Ru, and Ru^0 powders are shown in Supplementary Fig. 3. These powders, which were prepared by hydroxide precipitation and then thermally converted to oxides, did not exhibit a well-defined morphology. Agglomerates of 5–10 μm composed of nanometric UO_2 particles were observed either in the presence or in the absence of Ru. The 4 h heating treatment at 800 °C under Ar—H_2 caused the growth of Ru^0 grains (200 nm in diameter) and their sintering. The specific surface areas of the powdered samples measured by the BET method reached respectively 14.6 m^2 g^{-1}, 16.4 m^2 g^{-1}, and 5.4 m^2 g^{-1} for UO_2, UO_2/Ru, and Ru^0.

After sintering the powders, geometrical measurements, He pycnometry and SEM observations of the UO_2 and UO_2/Ru pellets were carried out to study the microstructure. The densification rate of the three UO_2 pellets used during the dissolution tests was high and almost similar (95–96% of the theoretical density, Table 1). The analysis of the SEM micrograph in Fig. 1a allowed determining an average UO_2 grains size of 3 μm. The densification rate of the UO_2/Ru pellet was lower than that of UO_2 (i.e., 89% of the theoretical density). The UO_2 grains were smaller with an average diameter and a standard deviation of 130 ± 60 nm. The

presence of nanometric particles is evidenced by the SEM at the highest magnification (Fig. 1b). They were homogeneously distributed at the UO₂/Ru pellet surface covering ~3% of the surface area of the image (Fig. 1c). Figure 1d shows the particles size distribution obtained by segmentation of several SEM images. From the analyses of thousands of particles, it appeared that their diameter ranged between 4 and 18 nm.

The SEM micrographs of the electron-transparent ultrafine cross-section cut from UO₂/Ru pellet (Fig. 2a) revealed the presence of nanometric particles of Ru (STEM-EDS spectrum provided in Fig. 2b) deep inside the pellet. The Ru nanoparticles were mainly located at the grains boundaries, and a few of them appeared in the UO₂ grains as well. STEM-EDS analysis confirmed that the nanoparticles were composed of metallic Ru. Low amounts of O and U were detected from the surrounding UO₂ grains.

Dissolution experiments

The experimental conditions associated with each dissolution test are summarised in Table 2. The behaviour of the UO₂ pellet during dissolution was considered as a reference to analyse the impact of ruthenium added under different forms to the various systems. The dissolution rate was systematically calculated to quantify this impact (Table 3). The kinetics of dissolution of UO₂ in $0.1 \, mol \, L^{-1}$ HNO_3 and in $0.1 \, mol \, L^{-1}$ HCl solutions at 60 °C at atmospheric pressure is represented in Fig. 3a. During the first 50 days (i.e., below 0.5% of relative mass loss), the dissolution rates in $0.1 \, mol \, L^{-1}$ HNO_3 solution were low (i.e., $9 \pm 2 \, \mu g \, d^{-1}$). In nitric acid solutions, this initial step was usually named "induction period" in the literature in which this slow kinetic regime was usually associated with a non-catalysed dissolution mechanism[18,19]. During the induction period in $0.1 \, mol \, L^{-1}$ HNO_3, the dissolution rate was similar to the one determined in $0.1 \, mol \, L^{-1}$ HCl (i.e., 9 ± 2 and $4 \pm 1 \, \mu g \, d^{-1}$, respectively). It was thus concluded that the dissolution rate was mainly controlled by the activity of the protons and of O_2 (aq) in the non-catalysed mechanism. Between 50 and 550 days, the dissolution rate was found to be significantly higher in HNO_3 than in HCl solution of the same acidity, with $76 \, \mu g \, d^{-1}$ and $4 \, \mu g \, d^{-1}$, respectively. A slight increase in the nitrous acid concentration was detected concomitantly to the increase of the dissolution rate in nitric acid (Fig. 3b). Nitrous acid is used in the literature as an indicator of the UO₂ auto-catalytic dissolution mechanism[18,25,26]. Nevertheless, the HNO_2 concentration remained much lower than the U elemental concentration in the solution (below $6.5 \times 10^{-5} \, mol \, L^{-1}$). It was therefore concluded that after 50 days of dissolution in $0.1 \, mol \, L^{-1}$ HNO_3 at 60 °C, the dissolution moved towards a weakly catalysed mechanism, while the dissolution mechanism remained unchanged for the entire duration of the experiment performed in HCl solution.

Figure 4 allows comparing the dissolution kinetics of UO₂/Ru and UO₂ pellets in $0.1 \, mol \, L^{-1}$ HNO_3 and HCl solutions at 60 °C. When the ruthenium metallic particles were incorporated into the UO₂ matrix, a strong increase in the dissolution rate was observed in both media. Indeed, the relative mass loss exceeded 90% after 20 and 35 days in HNO_3 and in HCl solutions, respectively. Compared to the reference UO₂, this result corresponded to an increase in the dissolution rate by a factor of 480 in HNO_3 and 450 in HCl. In addition, a very low concentration of nitrous acid ($<10^{-5} \, mol \, L^{-1}$) was measured during the complete dissolution of the UO₂/Ru pellet in $0.1 \, mol \, L^{-1}$ HNO_3 (Fig. 6b). Therefore, the catalytic effect observed in both media was attributed to the presence of the Ru^0 nanoparticles in contact with UO₂ in this system. Similar conclusions were already stated by Cordara et al.[17] when studying the dissolution kinetics of UO₂ pellets incorporating 3 mol.% of Ru particles under the same experimental conditions. However, according to Cordara et al.[17], the relative mass loss of UO₂ + 3 mol.% Ru pellet reached 19% after 20 days of dissolution in $0.1 \, mol \, L^{-1}$ HNO_3 solution at 60 °C against 90% in this work. The authors assumed that the positive impact of the PGM particles on the dissolution kinetics of UO₂ was linked to the reduction of nitrate ions to NOx at the particles/solution interface. The production of NOx at the pellet surface induced the fast dissolution of UO₂ due to the strong oxidative power of these species regarding to U(IV). Nevertheless, the production of NO_x and the subsequent formation of nitrous acid in solution were not detected in this work. Moreover, as the catalytic effect of the Ru^0 particles was also observed in HCl solution, it was assumed that other reactions were involved in the dissolution mechanism.

In order to improve our understanding of the role of Ru^0 particles, Ru was also introduced as Ru^0 particles in suspension in $0.1 \, mol \, L^{-1}$ HNO_3 (UO₂ + Ru^0 system) and as dissolved Ru(III) species (UO₂ + RuCl₃ and UO₂ + Ru nitrosyl systems). The goal of these experiments was to show if an intermediate Ru-based aqueous species was involved in the mechanism and responsible for the increase of the dissolution rate.

The results presented in Fig. 5a clearly show that the introduction of Ru^0 particles synthesised by the hydroxide route did not lead to an increase in the dissolution rate of UO₂ (the opposite effect was even observed). Indeed, the transition from

Table 1. Mass, geometrical surface area, porosities, and relative densities of the samples used in the dissolution tests.

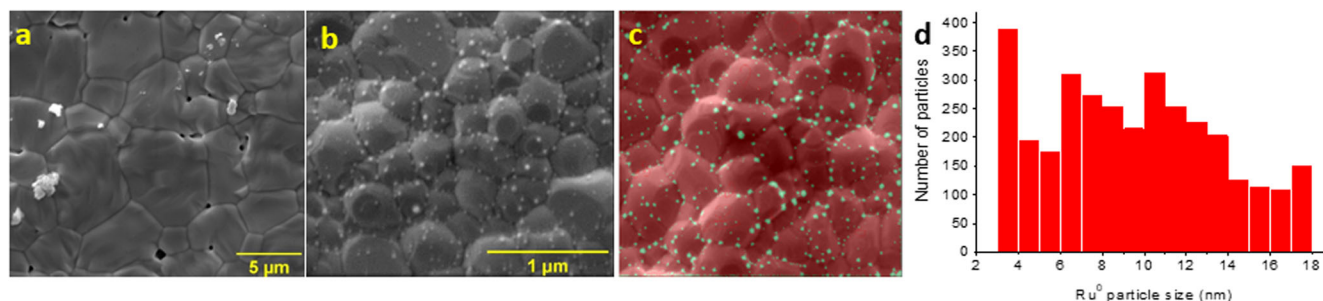| Sample code	Uncertainty	UO₂(1)	UO₂(2)	UO₂(3)	UO₂/Ru
m_0 (g)	±0.001	0.171	0.173	0.201	0.200
S_{geo} (cm²)	±0.005	0.016	0.016	0.019	0.020
d_{geo} (g/cm³)	±0.2	10.5	10.5	10.6	9.8
Densification rate (%)	±1	95	96	96	89
d_{pycno} 0.1 (g/cm³)	±0.1	10.8	10.8	10.6	10.7
P_{closed} (%)	±1	1.9	1.9	3.6	2.6
P_{open} (%)	±1	2.9	2.1	0.3	8.4

Fig. 1 Microstructural analysis of the model compounds by SEM. SEM micrographs of UO₂(1) pellet (**a**) and of UO₂/Ru pellet (**b**) in SE mode. Segmentation of the UO₂/Ru SEM micrograph (**c**) and Ru^0 particle size distribution calculated from several SEM images after segmentation (**d**).
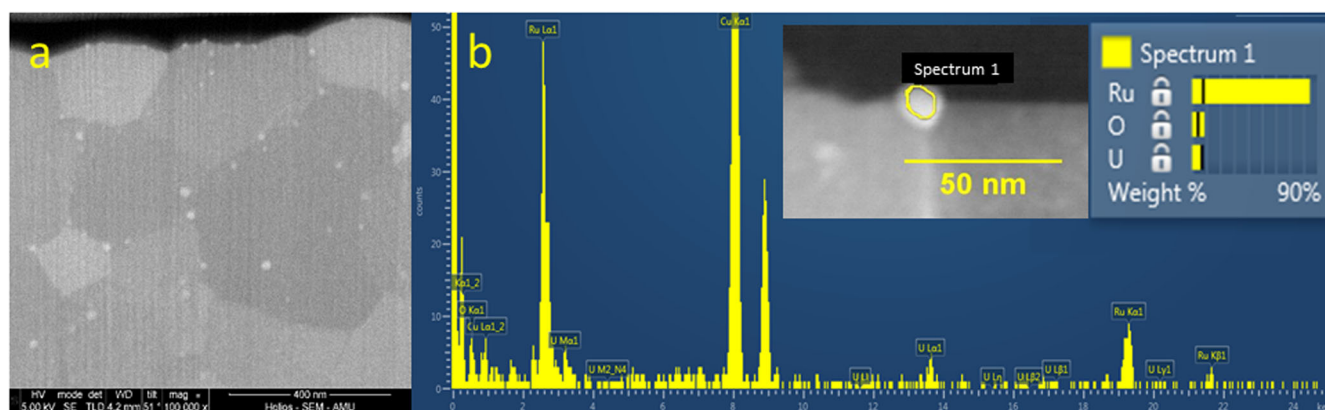
Fig. 2 Chemical analysis of the particles incorporated in the UO₂/Ru sample. SEM micrograph of an electron-transparent ultrafine cross-section cut by FIB in a UO₂/Ru pellet (**a**) in SE mode, STEM-EDS spectrum of a ruthenium particle in the UO₂/Ru FIB lamella (**b**).

Table 2. Summary of the experimental conditions used in the different dissolution tests.

System	UO$_2$		UO$_2$/Ru		UO$_2$+Ru^0	UO$_2$+Ru(III)		Ru^0
Sample code	UO$_2$(1)				UO$_2$(2)	UO$_2$(3)		–
Dissolution medium	0.1 M HNO$_3$	0.1 M HCl	0.1 M HNO$_3$	0.1 M HCl	0.1 M HNO$_3$	0.1 M HNO$_3$+ RuCl$_3$	0.1 M HNO$_3$+ Ru(NO)(NO$_3$)$_x$(OH)$_y$	0.1 M HNO$_3$
m_0 (UO$_2$) (mg)	80.3	77.2	92.6	70.9	92.1	76.5	62.7	–
m_0 (Ru^0) (mg)	–	–	1.58	1.23	1.37	–	–	11.4
C_{Ru} (mol L^{-1})	–	–	–	–	–	1.98×10^{-4}	1.58×10^{-4}	–

Table 3. Dissolution rate of UO$_2$ (R_d), duration of the experiment (t_{end}), and relative mass loss at the end of the experiment for the different systems studied in 0.1 mol L^{-1} HNO$_3$ or in HCl solution at 60 °C under air.

System	UO$_2$	UO$_2$	UO$_2$/Ru	UO$_2$/Ru	UO$_2$+Ru^0	UO$_2$+RuCl$_3$	UO$_2$+Ru nitrosyl
Sample code	UO$_2$(1)	UO$_2$(1)	UO$_2$/Ru	UO$_2$/Ru	UO$_2$(2)	UO$_2$(3)	UO$_2$(3)
Medium	HNO$_3$	HCl	HNO$_3$	HCl	HNO$_3$	HNO$_3$	HNO$_3$
R_d (µg d^{-1})	9*→76 ± 3	4 ± 1	4300 ± 130	1800 ± 50	6 ± 1	17 ± 1	11 ± 1
t_{end} (days)	618	618	35	35	536	71	71
Δm(U)/m_0 (%)	62 ± 2	4 ± 1	90 ± 2	91 ± 2	4 ± 1	2 ± 1	1 ± 1

*Means that the dissolution rate was calculated before 50 days.

the non-catalysed to the weakly catalysed mechanism observed for UO₂ after 50 days did not occur in the presence of Ru⁰ particles suspended in 0.1 mol L⁻¹ HNO₃ at 60 °C. Accordingly, the production of nitrous acid was completely inhibited (Fig. 5b) since the HNO₂ concentration remained close to the detection limit of the Griess method for the entire duration of the experiment (i.e., below 10⁻⁵ mol L⁻¹). Thus, the dissolution rate (Table 3) remained constant and close to the one measured for UO₂ during the induction period.

Figure 6a shows the evolution of the relative mass loss of UO₂ in the presence of 1.98×10^{-4} and 1.58×10^{-4} mol L⁻¹ of Ru introduced as RuCl₃ and Ru(NO)(NO₃)$_x$(OH)$_y$, respectively. Compared to the experiment performed with UO₂ in 0.1 mol L⁻¹ HNO₃, it appeared that the kinetics of dissolution was not strongly modified by the introduction of Ru(III) in solution regardless of its form. During the first 50 days of dissolution, the presence of Ru(III) in the solution introduced as nitrosyl species had no effect on the dissolution rate. After 50 days, it seemed that its presence slightly

inhibited the dissolution suggesting a potential impact of Ru(III) nitrosyl on the rate of formation of the catalytic species produced in the nitric acid solution during the induction period. A slightly different behaviour was observed when Ru(III) was added as RuCl₃ to the dissolution medium. Indeed, the dissolution rate was constant and initially slightly higher than in the absence of Ru. However, the increase of the dissolution rate evidenced in the absence of Ru was not observed after 50 days and hence confirming the potential inhibition of the formation or the consumption of the catalytic species produced when dissolving UO₂ in nitric acid. It is noteworthy that during the entire dissolution experiment, samples were taken to measure the HNO₂ concentration. However, the Griess reagent reacted with the ruthenium in solution, which resulted in inaccurate determinations. In parallel, the concentration of ruthenium solution was also monitored and was stable (Fig. 6b).

During the dissolution of each Ru⁰ particles containing system, the elemental Ru concentration was monitored in solution by ICP-
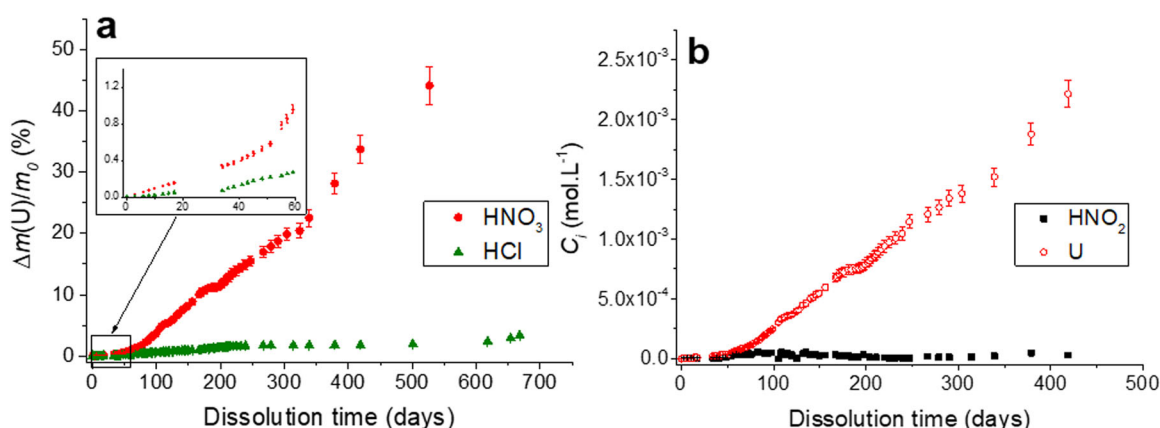
Fig. 3 Dissolution tests performed with the reference UO₂. Evolution of the relative mass loss of uranium during the dissolution of UO_2 in $0.1\,mol\,L^{-1}$ HNO_3 (red dots) and in $0.1\,mol\,L^{-1}$ HCl (green triangles) at 60 °C (**a**). Evolution of the concentration of uranium (red circles) and HNO_2 (black squares) during the dissolution of UO_2 in $0.1\,mol\,L^{-1}$ HNO_3 at 60 °C (**b**). Error bars are twice the standard deviation.
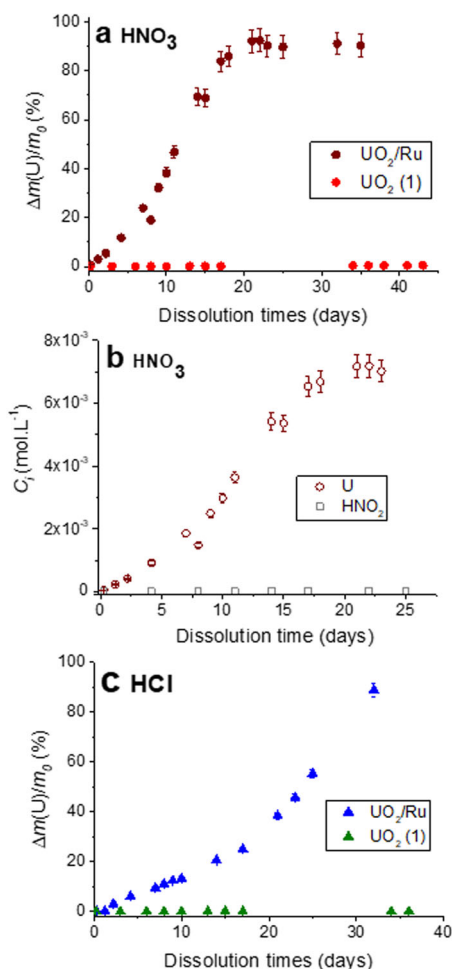

Fig. 4 Dissolution tests performed with the UO₂/Ru sample. Evolution of the relative mass loss of uranium during the dissolution of UO₂/Ru (brown dots) and UO₂ (red dots) pellets in $0.1\,mol\,L^{-1}$ HNO_3 at 60 °C (**a**). Evolution of the concentration of uranium (brown circles) and HNO_2 (grey squares) during the dissolution of UO₂/Ru pellet in $0.1\,mol\,L^{-1}$ HNO_3 at 60 °C (**b**). Evolution of the relative mass loss of uranium during the dissolution of UO₂/Ru (blue triangles) and UO₂ (green triangles) pellets in $0.1\,mol\,L^{-1}$ HCl at 60 °C (**c**). Error bars are twice the standard deviation.

MS measurements (Fig. 7). From the different evolutions of the elemental Ru concentration obtained, it appeared that ruthenium was detected in solution at a very low level. The maximum dissolved Ru concentration was $5 \times 10^{-7}\,mol\,L^{-1}$, measured for Ru^0 particles solely dissolved in $0.1\,mol\,L^{-1}$ HNO_3 solution (Fig. 7c). Depending on the experimental conditions, this concentration corresponded to the dissolution of 0.02 wt.% of Ru^0 particles after 180 days. Under the same conditions including the dissolution duration, only 0.002 wt.% of Ru^0 particles were dissolved in the presence of the UO_2 pellet (Fig. 7a). When Ru nanoparticles were incorporated in the UO_2 pellet (Fig. 7b), 0.01 wt.% of Ru^0 particles were dissolved after 24 days whereas the UO_2 matrix was entirely dissolved. In $0.1\,mol\,L^{-1}$ HCl solution (Fig. 7d), the dissolution of the Ru nanoparticles was low but slightly greater than that in $0.1\,mol\,L^{-1}$ HNO_3 with 0.05% after 34 days whereas the UO_2/Ru pellet dissolution was complete. The shape of the Ru nanoparticles dissolution curves differed in HNO_3 and HCl media following the shape of the U mass losses (Fig. 4a, c). This result suggested the existence of a link between the dissolution of the UO_2 matrix and of the Ru nanoparticles in the UO_2/Ru system. At this stage, we assumed that the dissolution of the UO_2 matrix released new Ru nanoparticles in solution that were initially embedded in the bulk pellet. Consequently, the surface area of Ru nanoparticles in contact with the acidic solution increased as the dissolution of the matrix progressed. This phenomenon could explain the difference observed between the shapes of the Ru^0 dissolution curves.

Undissolved residues were recovered at the end of the dissolution experiment of UO_2/Ru pellet in $0.1\,mol\,L^{-1}$ HNO_3 solution, then characterised by HR-TEM (Fig. 8). The presence of remaining small grains of UO_2 was evidenced in few places of the TEM grid, but the majority of the particles collected were spherical ruthenium nanoparticles (Fig. 8a, b) of 5–15 nm in diameter. This size range was in agreement with that of the Ru particles in the prepared UO_2/Ru pellet (Fig. 1d). Lattice fringes were clearly visible for the largest particles in this image, which underlined the crystalline nature of these particles. The selected area electron diffraction (SAED) pattern (Fig. 8b) showed the expected ring pattern for *hcp* ε-Ru metal. The SAED pattern consisted of discrete reflexions and diffuse bands. This suggested the presence of many crystallites of various orientations, which presented a significant degree of disorder. The determination of d-spacing from SAED image analysis was in agreement with the $P6_3/mmc$ space group, as for the Ru^0 particles synthesised in this work (Supplementary Fig. 1) and the 5 metals particles identified in the spent fuel[2,27]. Thus, the residues of dissolution of the UO_2/Ru pellet were mainly composed of *hcp* ε-Ru-metal nanoparticles with the same morphology and size as in the pristine pellet. The TEM
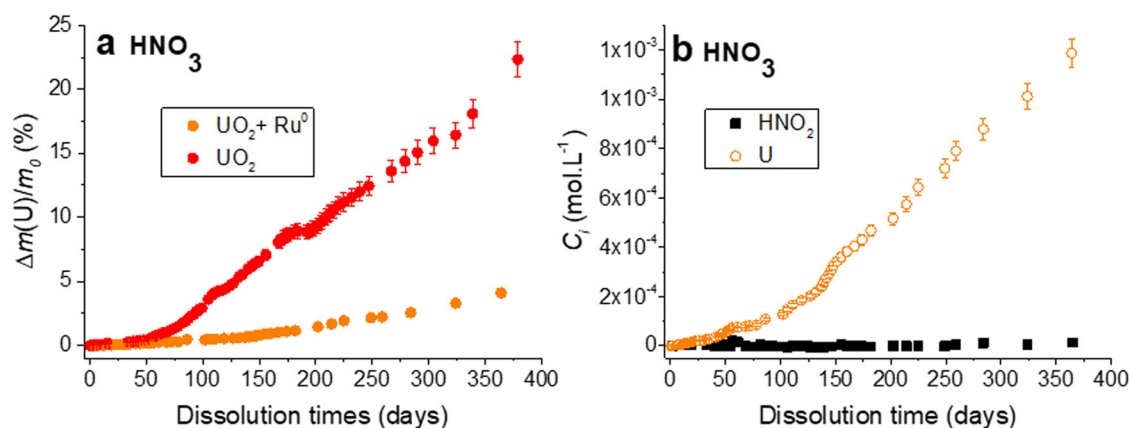
Fig. 5 Dissolution tests performed with the UO₂ + Ru⁰ system. Evolution of the relative mass loss of uranium (orange dots) (**a**) and of the concentration of uranium (orange circles) and HNO₂ (black squares) (**b**) during the dissolution of UO₂ + Ru⁰ system in 0.1 mol L⁻¹ HNO₃ at 60 °C. Error bars are twice the standard deviation.
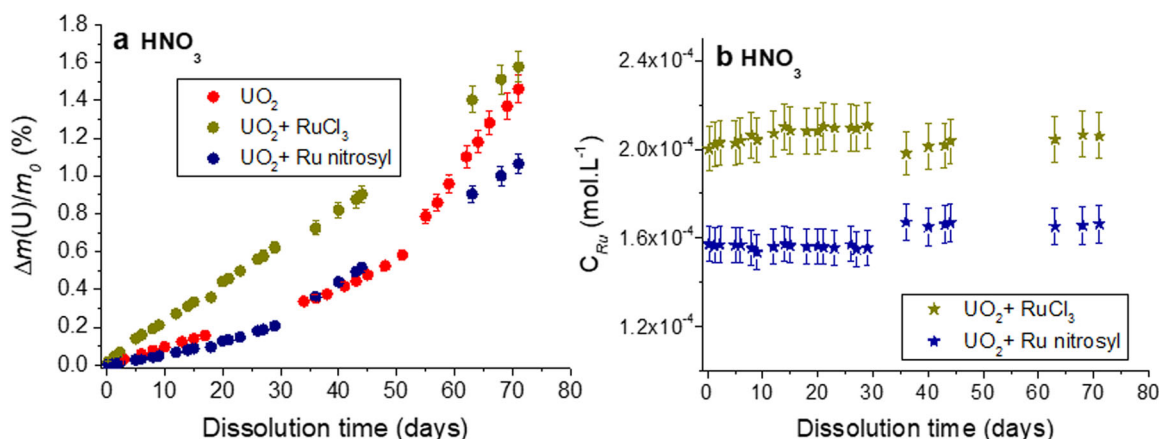

Fig. 6 Dissolution tests performed with UO₂ and aqueous species of Ru(III). Evolution of the relative mass loss of uranium during the dissolution of UO₂ in 0.1 mol L⁻¹ HNO₃ at 60 °C (red dots) in the presence of Ru in solution introduced as RuCl₃ (green dots) and Ru(NO)(NO₃)ₓ(OH)ᵧ (blue dots) (**a**). Evolution of the elemental concentration of Ru in solution during both dissolution experiments (**b**). Error bars are twice the standard deviation.

characterisations supported the idea that the Ru nanoparticles did not dissolve under the conditions used in this work or they could be dissolved too slowly leading to insignificant change.

Operando monitoring of the solid/liquid interface during the dissolution of UO₂/Ru pellet

In order to follow the evolution of the UO₂/Ru pellet microstructure during its dissolution in 0.1 mol L⁻¹ HNO₃ at 60 °C, the monitoring of the evolving solid/liquid interface was achieved by ESEM (Fig. 9). A similar methodology has already been used by Cordara et al.[20] or Podor et al.[28]. Briefly, several zones were located at the pellet surface before dissolution. The sample was removed from the dissolution medium several times, and washed with deionized water, then the selected zones were identified and directly observed at several magnifications under environmental conditions by ESEM, which allowed to follow the microstructure of the sample at different scales.

At a magnification of ×250 (Fig. 9a), it appeared that the initial cracks formed during the sintering step and the damaged zones associated with grain pull-outs were preferential dissolution zones. These zones were expanding and digging with the progress of the reaction, creating large paths for the fluid to enter the pellet. Preferential dissolution zones were also visible at ×5000

magnification (Fig. 9b). The evolution of an existing pore was clearly evidenced in this sequence of images.

At the highest magnification (×40,000, Fig. 9c), the UO₂ grains and the Ru nanoparticles became identifiable (see also Supplementary Fig. 4). At this scale, we noticed that the dissolution led to the spacing, and rounding of the UO₂ grains, and finally to their disappearance either by grain detachment from the surface of the pellet or by dissolution (between 0 and 20 h). At this observation scale, the dissolution appeared to be rather homogeneous even if the grain boundaries seemed to be attacked first. This observation was probably connected to the spatial distribution of Ru nanoparticles that were homogeneously distributed within and between the UO₂ grains (Fig. 1). Moreover, the ruthenium nanoparticles were always visible at the highest magnification and their number increased with the progress of the dissolution. The Ru nanoparticles were agglomerating and covering an increasingly large surface area of the grains. This progressive covering of the pellet surface by the Ru nanoparticles indicated that the particles released by dissolution of the first layers of UO₂ grains were re-deposited at the pellet surface without dissolving themselves. This observation was in agreement with the low concentration of dissolved Ru measured in the bulk solution during this experiment (Fig. 7b).
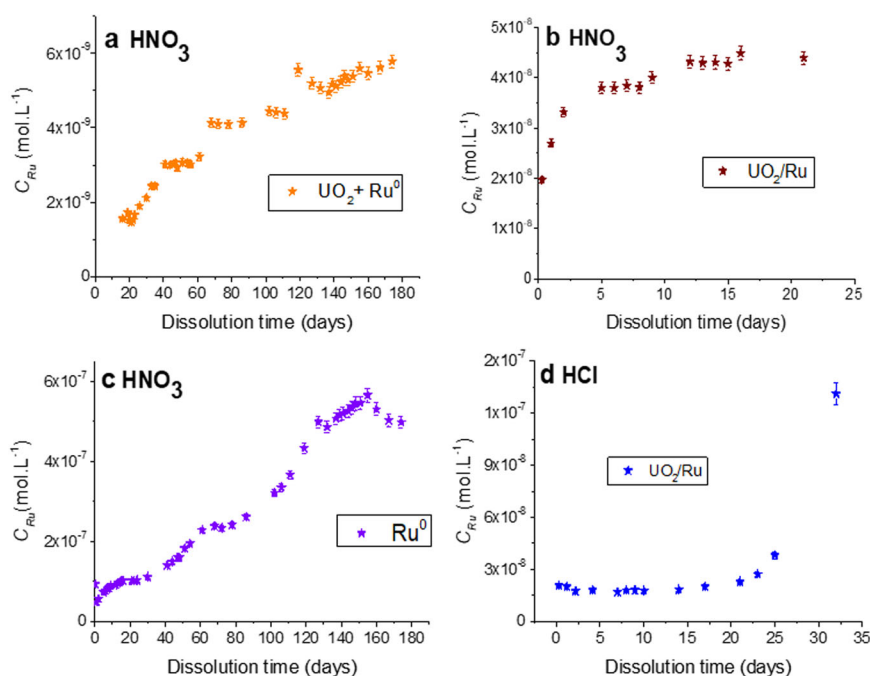
Fig. 7 Dissolution of Ru⁰ particles in the different systems. Evolution of the elemental Ru concentration during the dissolution of $UO_2 + Ru^0$ system (**a**), UO_2/Ru pellet (**b**), Ru^0 particles alone (**c**) in 0.1 mol L^{-1} HNO_3 at 60 °C and of UO_2/Ru pellet in 0.1 mol L^{-1} HCl at 60 °C (**d**). Error bars are twice the standard deviation.

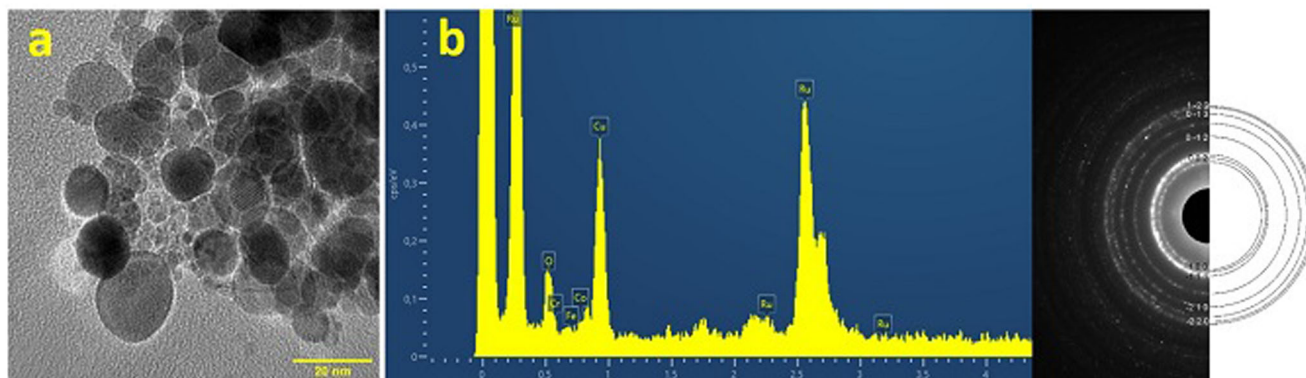**Fig. 8 Characterisation of dissolution residues by TEM.** HR-TEM image of residues obtained after the dissolution of UO_2/Ru pellet in 0.1 mol L^{-1} HNO_3 60 °C (**a**) EDS spectrum and SAED pattern of the residues (**b**).

DISCUSSION

The results obtained in this work confirmed the previous findings made by Cordara et al.[17]. In 0.1 M HNO_3 at 60 °C, the authors found the dissolution rate of UO_2/Ru with 3 mol.% of Ru was 1124 ± 120 µg d^{-1} [17]. This value was found to be 355 times higher than the dissolution rate of UO_2. They demonstrated that Rh and Pd metallic particles incorporated at 3 mol.% in UO_2 also influenced the kinetics of dissolution. The dissolution rate of UO_2/Rh and UO_2/Pd pellets were 115 and 93 times higher than that of UO_2, respectively. This result led the authors to conclude that among the PGM elements studied, ruthenium had the strongest effect on the dissolution kinetics of UO_2. Interestingly, the dissolution rate of UO_2 incorporating 3 mol.% of PGM particles was found to be 173 ± 20 µg d^{-1}, which is only 55 times higher than UO_2. The PGM particles contained 36 mol.% of Pd, 10 mol.% of Rh, and 54 mol.% of Ru. Thus, the metallic alloy of PGM had a lower effect on the UO_2 dissolution rate than the weighted sum of the effects of each element. It is important to note that in the study reported by Cordara et al.[17], the Ru particles were the smallest ones with an average diameter of less than 10 nm against almost 100 nm for the PGM mixture, Rh, and Pd particles. The nanometric dimension of the Ru particles could contribute to enhancing their reactivity and increasing their impact on the dissolution rate compared to the PGM, Rh, and Pd particles.

The dissolution rate of UO_2/Ru determined by Cordara et al.[17] in 0.1 M HNO_3 at 60 °C was 1124 ± 120 µg d^{-1}. This value was of the same order of magnitude, but lower than the one obtained in this work under similar conditions (i.e., $R_d = 4300 \pm 130$ µg d^{-1} in Table 3). The microstructure of the UO_2/Ru pellets can explain such a discrepancy. Indeed, Cordara et al.[17] prepared a pellet with a densification rate of 93%, 2% of open porosity, and 5% of closed porosity. The UO_2/Ru pellet dissolved in this work showed a lower densification rate of 90%, and above all a higher open porosity of 8% (Table 1). Open porosity was mainly caused by the presence of numerous cracks formed during the thermal treatment of sintering. The presence of this cracks network could contribute
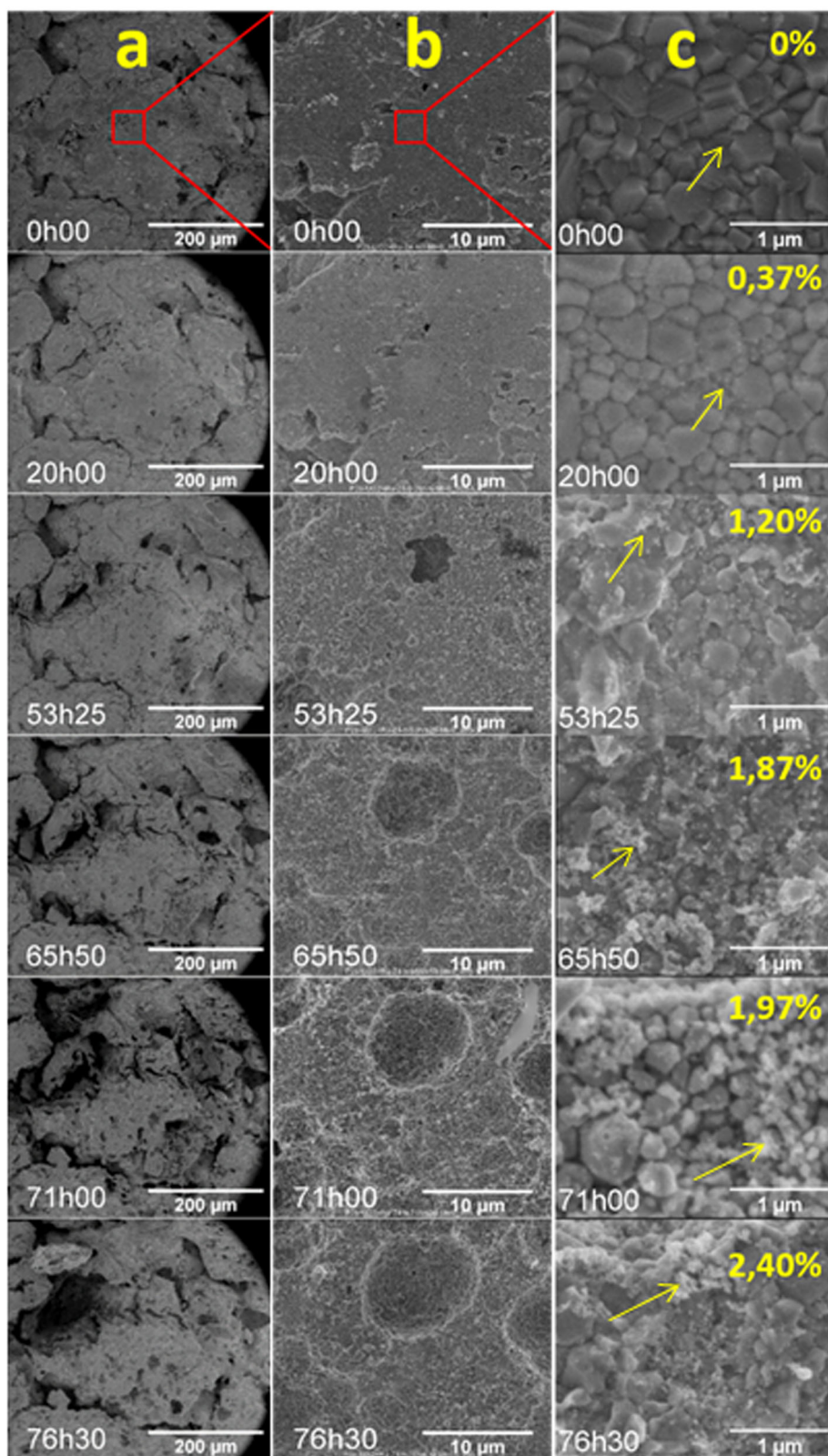
Fig. 9 ESEM monitoring of the UO$_2$/Ru pellet during dissolution. SEM micrographs of the surface of the UO$_2$/Ru pellet during dissolution test performed in 0.1 mol L^{-1} HNO$_3$ at 60 °C for different dissolution times and at various magnifications (**a** ×250, **b** ×5000, and **c** ×40000) in SE mode. The relative mass loss of UO$_2$ is indicated in each micrograph. At the highest magnification, arrows show examples of Ru particles or agglomerates of particles.
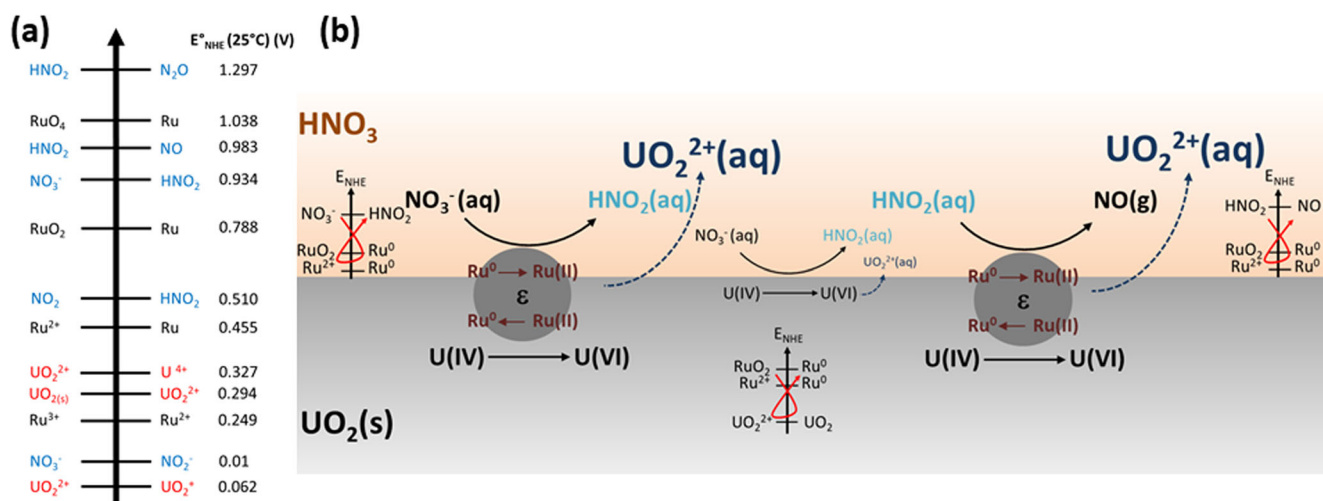
Fig. 10 Schematic model of the catalytic dissolution of UO₂/Ru. Redox potentials vs NHE of selected redox couples at 25 °C taken from[21] except for $UO_2^{2+}/UO_{2(s)}$ calculated from[22] (**a**). A proposed mechanism that explains the catalytic effect of Ru^0 nanoparticles incorporated in the UO_2 matrix (**b**) during dissolution in nitric acid.

to the increase of the reactive surface area of the UO₂/Ru pellet compared to the pellet dissolved by Cordara et al.[17], and thus could be responsible for the different dissolution rates. The R_d measured in this work for the UO₂/Ru pellet was 4 times higher than the value determined by Cordara et al.[17]. The UO₂ pellet used as a reference in this work to quantify the impact of the Ru particles had an open porosity of 2.9%. Following the same reasoning, the increase of the reactive surface area of the UO₂/Ru pellet cannot explain on its own the acceleration factor of 480 obtained when comparing the dissolution rate of UO₂/Ru and UO₂ pellets. This strong increase was mainly caused by the introduction of Ru metallic particles.

The evolution of the global elemental Ru concentration during the dissolution of the UO₂/Ru pellet (including Ru from UO₂ + Ru (III) system) demonstrated unambiguously that the dissolved Ru (III) species were not responsible for the strong increase of UO₂ dissolution rate in the UO₂/Ru system neither in the 0.1 mol L⁻¹ HNO₃ nor in the HCl solutions at 60 °C. TEM characterisation of the dissolution residues also showed that the dissolution of Ru^0 particles was limited in the carried conditions, which confirmed that the various pseudo-octahedral complexes of Ru nitrosyl with the general formula $[Ru(NO)(NO_3)_x(NO_2)_y(OH)_z(H_2O)_{5-x-y-z}]^{3-x-y-z}$ were formed at a very low concentration level. However, introducing these species in the dissolution media at a high concentration level (as in UO₂ + Ru(III) systems) did not allow to accelerate significantly the rate of dissolution of UO₂. These observations suggested that the dissolution of Ru nanoparticles was not required to promote the dissolution of UO₂. In addition, the results obtained for the UO₂ + Ru^0 system also suggested that the reaction between Ru^0 particles and HNO₃ rather led to the decrease of the UO₂ dissolution rate by decreasing the concentration of the catalytic species produced at the HNO₃/UO₂ interface in the bulk solution. The existence of UO₂/Ru^0 interface was thus necessary to induce the catalytic effect, as neither aqueous Ru (III) species nor the solutes formed at the HNO₃/Ru^0 interface that could be transported at the UO₂ surface, were involved in the catalytic mechanism.

Given the complex redox chemistry of the UO₂/Ru pellet dissolved in nitric acid, many reactions are likely to support our observations. In order to illustrate this complex redox chemistry, the redox potentials of several couples of interest are provided in Fig. 10a. Several key points emerged from this work. Firstly, Ru^0 particles were not dissolved and Ru (III) aqueous species were not involved in the catalytic mechanism. Secondly, isolated Ru^0

particles did not reduce nitrate ions to form nitrogen-based species in solution with a higher oxidising power towards U(IV), which could then react with UO₂ and would increase its dissolution rate. Although this reaction is thermodynamically possible (Fig. 10a), it would be kinetically limited, or the reaction product (i.e., HNO₂) would be consumed in another redox reaction involving Ru. This latter reaction would explain the absence of nitrous acid in the HNO₃ solution during the dissolution of the UO₂/Ru pellet and UO₂ + Ru^0 system. Nevertheless, the absence of HNO₂ was associated with drastically different dissolution regimes when the Ru^0 particles were in suspension in the bulk solution (UO₂ + Ru^0 system) or in contact with the UO₂ matrix (UO₂/Ru pellet). In the UO₂ + Ru^0 system, the absence of HNO₂ induced the extension of the induction period. For the UO₂/Ru pellet, this induction period did not exist and a catalytic dissolution regime was achieved despite the very low amount of HNO₂ in the solution.

Figure 10b gives a schematic representation of a potential mechanism based on the above-mentioned observations. The key phenomenon that would support the catalytic impact was connected to the oxidation of Ru^0 in Ru (II) entities by nitrate ions and the concomitant reduction of Ru (II) at the particle/UO₂ interface, leading eventually to the formation of NO(g) and U (VI). The speciation of Ru (II) in these entities remained unknown. However, the examination of the standard potentials of the RuO₂/Ru or Ru^{2+}/Ru couples revealed that the intermediate species RuO₂ could be involved in this mechanism, even if Ru^{2+} appeared thermodynamically favoured. U (VI) reactive sites were further solubilized as UO_2^{2+} species at the UO₂/solution interface. The electronic transfer from the solution to UO₂ was promoted by the high electric conductivity of the metallic particles, their nanometric dimension as well as the mutual contact with UO₂. This phenomenon was further amplified by the increase of the surface coverage of the pellet by Ru^0 nanoparticles with the dissolution progress as observed during the monitoring of the UO₂/Ru interface by ESEM.

It is worth noting that the main product of the reduction of nitrates at the Ru^0/nitric acid solution interface has not been identified yet although NO(g) is one of the potential candidates. This species was analysed by Hermann[29] and Glatz et al.[30] in off-gases during the dissolution of UO₂ in concentrated nitric acid solutions, and appeared as the major component of the off-gases for $[HNO_3] < 7$ mol L⁻¹ [31]. The appearance of NO_x bubbles has been also observed by Marc et al.[32] using an optical microscope

during the dissolution of a UO_2 pellet in 4.93 mol L^{-1} HNO_3. The formation of gas bubbles in more diluted HNO_3 solutions has never been observed. Considering the detection limit of the analytical techniques reported in the literature, the identification of NO(g) is challenging in the experimental conditions used in this work but its detection would definitely confirm the suggested mechanism associated with the catalytic impact of Ru^0 nanoparticles incorporated in the UO_2 pellet.

Even if the proposed mechanism could explain the catalytic effect of Ru^0 nanoparticles during the dissolution of UO_2 in nitric acid, it could not exist in hydrochloric acid, although an acceleration of the dissolution was also observed in this medium. Different redox couples should be involved in HCl. One possibility could be that Ru metallic particles catalyse the oxidation of U (IV) to U (VI) in the presence of O_2. H_2O_2 might be also produced by the concomitant reduction of O_2. Among the water radiolysis products, H_2O_2 was reported as the most important oxidant with respect to UO_2[33]. In addition, Clarens et al.[34] also reported that UO_2 dissolution rate in the presence of 10^{-5} mol L^{-1} of H_2O_2 increased by 2 orders of magnitude when the pH of the solution decreased from 7 to 3.5. Under acidic conditions, the solubilisation of U(VI) entities at the UO_{2+x} solid/solution interface would no longer be the rate-limiting step in the oxidative-dissolution mechanism. Although the formation of oxygen peroxide is not required to explain the acceleration of the dissolution of UO_2 in aerated media, it is monitoring at the trace level could be possible using chemiluminescence[35].

Thus, the effect of Ru-metal particles incorporated at a level of 3 mol.% in UO_2 pellet on the dissolution rate was evident in both nitric and hydrochloric acid solutions. The obtained results unambiguously demonstrated the catalytic activity of Ru-metal particles during UO_2 dissolution in nitric acid based on a solid/solid interface existing between UO_2 and Ru-metal particles. Under the weak acid conditions (0.1 mol L^{-1} HNO_3 at 60 °C), the Ru-metal particles were virtually not dissolved and easily recovered in the dissolution residues, whereas the UO_2 dissolution rate was found to increase by a factor of 480. This positive impact on the dissolution kinetics of UO_2 was supported by redox reactions taking place at both nitric acid solution/Ru-metal particles and at Ru-metal particles/UO_2 interfaces. The magnitude of this impact is expected to be smaller in acid conditions more representative of the PUREX process. For this reason, the model compounds prepared in this work will be further submitted to dissolution tests in more aggressive media in order to evaluate the behavior of the Ru-metal particles as well as to establish an accurate Ru mass balance in the different flows generated by the PUREX process.

METHODS

Preparation of UO_2, UO_2/Ru pellets, and Ru^0 powder

Uranium dioxide powder was prepared by hydroxide precipitation according to the protocol initially developed by Martinez et al.[36]. This route consisted in pouring 3.42 g of uranium chloride stock solution (4.78×10^{-4} mol$_U$ g^{-1}) into a large excess of ammonium hydroxide solution at room temperature. Precipitation was found to be instantaneous. The precipitate was aged in solution for 30 min under magnetic stirring. Then the precipitated solid was separated from the supernatant by centrifugation at $5660 \times g$. The supernatant was analysed by ICP-OES to check that the precipitation of U and Ru was complete. The resulting powder was finally washed twice with deionised water and once with ethanol to remove all traces of ammonia. After this washing step, it was dispersed in 50 mL of ethanol. This suspension was then placed in the oven at 90 °C. The hydroxide precursor was finally converted to the oxide form by heating at 800 °C for 4 h under a reducing atmosphere (Ar—5% H_2).

The synthesis of UO_2/Ru powder was carried out following the same route. The uranium stock solution was first mixed with a 0.120 mol L^{-1} ruthenium solution prepared by dissolution of $RuCl_3$ (Sigma Aldrich, 99.9%)

in 1 mol L^{-1} hydrochloric acid. Uranium and ruthenium solutions were weighted to obtain the appropriate stoichiometry of Ru/U = 0.03. Dense pellets were prepared by sintering the UO_2/Ru calcinated powder. For that purpose, the powder was first deagglomerated in an agate mortar. Then, a three-shell die with a diameter of 5 mm was used to uniaxially press 180–200 mg of the powder at 500 MPa. Raw pellets of 1–2 mm thickness were produced. The raw pellets were sintered for 8 h at 1500 °C in a reducing atmosphere (Ar—5% H_2).

Finally, the synthesis of Ru particles was achieved by pouring the Ru stock solution alone into a large excess of ammonium hydroxide solution. The precipitate was washed, then heated at 800 °C for 4 h under a reducing atmosphere (Ar—5% H_2). The resulting powders and the dense pellets were characterised as described below.

Characterisations of the prepared samples

All the synthesised powders were characterised prior to sintering by PXRD, by N_2(g) or Kr(g) adsorption using the BET method (Brunauer, Emmet, and Teller), and by scanning electron microscopy (SEM) in secondary electron (SE) mode and beam intensity of 10 kV.

The microstructural characterisation of the prepared pellets was achieved before dissolution experiments. A detailed description of the procedure is available in the Supplementary Information file. Briefly, the density of the UO_2 and UO_2/Ru sintered pellets was determined using a caliper for geometrical measurements and helium pycnometry (Micrometrics, AccuPyc II 1340). SEM micrographs of the UO_2 and UO_2/Ru pellets were obtained using an FEI Quanta 200 apparatus equipped with a SE detector. The Fiji software was used to perform images analyses. Especially the size distribution of the UO_2 grains and Ru^0 particles was determined. Finally, an electron-transparent ultrafine cross-section was cut in a UO_2/Ru pellet prior to dissolution with a focused ion beam (FIB), FEI Helios 600 Nanolab (CP2M, Marseille, France). The FIB lamella was analysed by TEM, SEM, and energy dispersive X-ray spectroscopy (STEM-EDS) on FEI Tecnaï G2, equipped with a LaB6 source operating at 200 kV. STEM-EDS analyses were collected with a spot size of 5 nm, a tilt angle of 20°, and an acquisition time of 120 s.

After each dissolution experiment, the residues were recovered by centrifugation at $5660 \times g$ for 5 min and stored in ethanol for further analysis. The analysis of the dissolution residues was carried out by high-resolution transmission electron microscopy (HR-TEM), using a JEOL 2200FS-200 kV employed at the MEA platform (University of Montpellier). STEM-EDS analyses were obtained with a spot size of 0.7 nm on an Oxford Instrument X-MaxN 100 TLE EDX detector.

Dissolution experiments

Dissolution tests were carried out at 60 °C under static conditions with mechanical stirring, using 60 mL PFA reactors (Savillex). For the UO_2 and UO_2/Ru systems, half a pellet was placed in 50 mL of 0.1 mol L^{-1} HNO_3 solution and the other half in 50 mL of a 0.1 mol L^{-1} HCl solution. For the UO_2 + Ru^0 system, 1.37 mg of ruthenium particles (synthesised by hydroxide route) were added to the 50 mL of 0.1 mol L^{-1} HNO_3 solution in contact with the UO_2 pellet. This amount corresponded to Ru/U ratio of 3 mol.%. The same experiment was conducted without UO_2 pellet (Ru^0 system). For the UO_2 + Ru(III) system, Ru (III) was added to the 0.1 mol L^{-1} HNO_3 solution in contact with the UO_2 pellet up to 1.98×10^{-4} mol L^{-1} by dissolving a $RuCl_3$ salt (Sigma Aldrich, 99.9%). Finally, a similar experiment was carried out with 1.58×10^{-14} mol L^{-1} of Ru (III) added to the dissolution medium by diluting a commercial Ru nitrosyl nitrate solution (Ru(NO) $(NO_3)_x(OH)_y$, where $x + y = 3$ at 1.5 wt.% Ru from Sigma Aldrich). The experimental conditions associated with each dissolution test are summarised in Table 2.

At regular time intervals, 5 mL of solution was sampled and replaced by the same volume of fresh solution with the appropriate composition. After dilution with a 0.2 mol L^{-1} HNO_3 solution (prepared by dilution of 65% HNO_3 Suprapur, for trace analysis, Merck), the U elemental concentration was analysed in the collected samples by inductively coupled plasma atomic emission spectroscopy (ICP-AES, Spectro Arcos). The intensities of the emission peaks were recorded at $\lambda = 279.394$ nm, 367.007 nm, and 409.014 nm. The ICP-AES was calibrated against standard solutions prepared by diluting a certified 1000 mg$_U$ L^{-1} standard solution (Plasma-CAL, SCP Science) in 0.2 mol L^{-1} HNO_3. The U elemental concentration was then calculated as the average of the three measurements replicates at each wavelength. The experimental uncertainty was estimated as twice the standard deviation of the nine uranium elemental concentration

measurements. The ruthenium elemental concentration was measured by an ICP-MS (iCAP RQ, Thermo Fisher) calibrated for [101]Ru, [102]Ru, and [104]Ru isotopes, using several standard solutions prepared by diluting 1000 mg$_{Ru}$ L^{-1} standard solution (PlasmaCAL, SCP Science) and 0.2 mol L^{-1} HNO$_3$ solution (Suprapur, for trace analysis Merck). In addition, [193]Ir and [209]Bi were used as internal standards. The concentration of elemental ruthenium was calculated from the average mass of three replicates. The experimental uncertainty was estimated as twice the standard deviation of the nine Ru elemental concentration measurements. Under these analytical conditions, the detection limit of uranium and ruthenium reached 2×10^{-7} mol L^{-1} and 1×10^{-10} mol L^{-1}, respectively. For the dissolution performed in 0.1 mol L^{-1} HCl solution, the sampling procedure was similar, but the uranium concentration was determined by alpha scintillation (PERALS spectrometer) by Alphaex scintillation cocktail and the protocol described in Dacheux et al.[37].

The relative mass of dissolved material, $\Delta m(i)/m_0$ (in wt.%) was calculated using the elemental concentration as follows:

$$\frac{\Delta m(i)}{m_0} = \frac{m_i(t)}{f_i \times m_0} \times 100 = \frac{C_i(t) \times V}{f_i \times m_0} \times 100 \qquad (2)$$

where $m_i(t)$ (g) corresponds to the total amount of the element i released in the solution at time t calculated from the elementary concentration, $C_i(t)$ (g L^{-1}), and the volume of solution in contact with the solid, V (L). In this expression, f_i (g g^{-1}) is the mass fraction of the element i in the solid and m_0 is the initial mass of the solid phase (g).

The dissolution rate R_d, expressed in g d^{-1}, was obtained by linear regression of the dissolution curve, $\Delta m(U)$. The uncertainty associated with the dissolution rate value was estimated as twice the standard error on the slope of the fitted linear function.

During the dissolution of sintered pellets of UO$_2$ and UO$_2$/Ru in 0.1 mol L^{-1} HNO$_3$ solution, the nitrous acid concentration in the solution was measured in selected samples. In order to stabilise nitrous acid as nitrite ions and to avoid any interference with uranyl in the UV-visible spectra, the 5 mL aliquots were first basified by adding 1 mL of 8 mol L^{-1} NaOH solution. After centrifugation and acidification of the supernatant at a pH = 2 with 8 mol L^{-1} H$_2$SO$_4$ solution, the Griess method was used (Nitrite Test Spectroquant®, Merck). The nitrite ions concentration was measured by UV-Visible spectroscopy. The violet complex formed with nitrite ions had a wide, non-interfering absorbance band at 540 nm. Quantitative analyses were made by calibrating the UV-vis spectrometer, using several solutions prepared by diluting a certified NaNO$_2$ standard solution (NIST standard solution, CertiPUR® Merck). Prior to dissolution, HNO$_2$ measurements were carried out in fresh nitric acid solutions. The concentration of nitrous acid was below the detection limit of the method, i.e., 5×10^{-6} mol L^{-1}.

DATA AVAILABILITY

The data sets generated during and/or analysed during the current study are available from the corresponding author on reasonable request.

REFERENCES

1. Kleykamp, H. The chemical-state of the fission-products in oxide fuels. *J. Nucl. Mater.* **131**, 221–246 (1985).
2. Cui, D. et al. Characterization of alloy particles extracted from spent nuclear fuel. *J. Nucl. Mater.* **420**, 328–333 (2012).
3. Swain, P., Mallika, C., Srinivasan, R., Mudali, U. K. & Natarajan, R. Separation and recovery of ruthenium: a review. *J. Radioanal. Nucl. Chem.* **298**, 781–796 (2013).
4. Lefebvre, C. et al. Addressing ruthenium speciation in tri-n-butyl-phosphate solvent extraction process by fourier transform infrared, extended X-ray absorption fine structure, and single crystal X-ray diffraction. *Ind. Eng. Chem. Res.* **56**, 11292–11301 (2017).
5. Siczek, A. A. & Steindler, M. J. Chemistry of ruthenium and zirconium in the PUREX solvent-extraction process. *At. Energy Rev.* **16**, 575–618 (1978).
6. Dirks, T., Dumas, T., Guillaumont, D. & Charbonnel, M. C. Coupling Raman spectroscopy and DFT study for enhanced description of nitrosyl nitrato nitrite ruthenium(III) complexes in nitric acid. *J. Radioanal. Nucl. Chem.* **326**, 1213–1223 (2020).
7. Kato, A., Kaneko, M. & Nakashima, S. Complexation and bonding studies on [Ru(NO)(H$_2$O)$_5$]$^{3+}$ with nitrate ions by using density functional theory calculation. *RSC Adv.* **10**, 24434–24443 (2020).
8. Holm, J., Glanneskog, H. & Ekberg, C. Deposition of RuO$_4$ on various surfaces in a nuclear reactor containment. *J. Nucl. Mater.* **392**, 55–62 (2009).
9. Kleiman-Shwarsctein, A. et al. A general route for RuO$_2$ deposition on metal oxides from RuO$_4$. *Chem. Comm.* **48**, 967–969 (2012).
10. Laurin, C. et al. Redox behavior of ruthenium in nuclear glass melt: ruthenium dioxide reduction reaction. *J. Nucl. Mater.* **545**, 152650 (2021).
11. McNamara, B. K. et al. Separation of metallic residues from the dissolution of a high-burnup BWR fuel using nitrogen trifluoride. *J. Fluor. Chem.* **162**, 1–8 (2014).
12. Adachi, T. et al. Dissolution study of spent PWR fuel - dissolution behavior and chemical-properties of insoluble residues. *J. Nucl. Mater.* **174**, 60–71 (1990).
13. Lausch, J. et al. Dissolution residues of highly burnt nuclear-fuels. *J. Nucl. Mater.* **208**, 73–80 (1994).
14. Wronkiewicz, D. J., Watkins, C. S., Baughman, A. C., Miller, F. S. & Wolf, S. F. Corrosion testing of a simulated five-metal epsilon particle in spent nuclear fuel, in *Scientific Basis for Nuclear Waste Management XXV* 625–632 (Materials Research Society Symposium Proceedings vol. 713, B. P. McGrail & G. A. Cragnolino, 2002).
15. Cui, D., Low, J., Sjöstedt, C. & Spahiu, K. On Mo-Ru-Tc-Pd-Rh-Te alloy particles extracted from spent fuel and their leaching behavior under Ar and H$_2$ atmospheres. *Radiochim. Acta* **92**, 551–555 (2004).
16. Ikeda, Y., Yasuike, Y., Takashima, Y., Nishimura, K. & Hasegawa, S. Acceleration effect of noble-metals on dissolution rate of UO$_2$ powders in nitric-acid. *J. Nucl. Sci. Technol.* **30**, 485–487 (1993).
17. Cordara, T. et al. Impact of platinum group metals (Ru, Pd, Rh) on the dissolution of UO$_2$. *J. Nucl. Mater.* **528**, 151836 (2020).
18. Bertolotto, S. et al. Effect of surface orientation on dissolution rate and surface dynamics of UO$_2$ single crystals in nitric acid. *Corr. Sci.* **176**, 109020 (2020).
19. Cordara, T. et al. Kinetics of dissolution of UO$_2$ in nitric acid solutions: a multiparametric study of the non-catalysed reaction. *J. Nucl. Mater.* **496**, 251–264 (2017).
20. Cordara, T. et al. Microstructural evolution of UO$_2$ pellets containing metallic particles of Ru, Rh and Pd during dissolution in nitric acid solution: 3D-ESEM monitoring. *Hydrometallurgy* **188**, 182–193 (2019).
21. Vanýsek, P. *CRC Handbook of Chemistry and Physics*. 91st edn, (CRC Press, Bocca Raton, FL., 2010).
22. Berger, P. Study of the mechanism of the dissolution of actinide's dioxides (UO$_2$, NpO$_2$ PuO$_2$, AmO$_2$) by chemical or electrochemical redox reactions in aqueous acid medium. *CEA, Tech. Rep.* **CEA-R-5515**, 234 (1988).
23. Kim, E. H. et al. Dissolution of UO$_2$ by photochemical reaction. *Radiochim. Acta* **83**, 147–151 (1998).
24. Leinders, G., Cardinaels, T., Binnemans, K. & Verwerft, M. Accurate lattice parameter measurements of stoichiometric uranium dioxide. *J. Nucl. Mater.* **459**, 135–142 (2015).
25. Shabbir, M. & Robins, R. G. Kinetics of dissolution of uranium dioxide in nitric acid. *J. Appl. Chem.* **18**, 129 (1968).
26. Desigan, N. et al. Mechanism of dissolution of nuclear fuel in nitric acid relevant to nuclear fuel reprocessing. *J. Radioanal. Nucl. Chem.* **312**, 141–149 (2017).
27. Buck, E. C., Mausolf, E. J., McNamara, B. K., Soderquist, C. Z. & Schwantes, J. M. Nanostructure of metallic particles in light water reactor used nuclear fuel. *J. Nucl. Mater.* **461**, 236–243 (2015).
28. Podor, R. et al. 3D-SEM height maps series to monitor materials corrosion and dissolution. *Mater. Charact.* **150**, 220–228 (2019).
29. Hermann, B. Dissolution of unirradiated UO$_2$-pellets in nitric acid. *KIT Tech. Doc.* **KFK- 3673**, 197 (1984).
30. Glatz, J. P., Bokelund, H. & Zierfuss, S. Analysis of the off-gas from dissolution of nuclear oxide fuels and carbide fuels in nitric-acid. *Radiochim. Acta* **51**, 17–22 (1990).
31. Marc, P., Magnaldo, A., Vaudano, A., Delahaye, T. & Schaer, É. Dissolution of uranium dioxide in nitric acid media: what do we know? *EPJ Nucl. Sci. Technol.* **3**, 13 (2017).
32. Marc, P., Magnaldo, A., Godard, J. & Schaer, É. A method for phenomenological and chemical kinetics study of autocatalytic reactive dissolution by optical microscopy. The case of uranium dioxide dissolution in nitric acid media. *EPJ Nucl. Sci. Technol.* **4**, 2 (2018).
33. Ekeroth, E., Roth, O. & Jonsson, M. The relative impact of radiolysis products in radiation induced oxidative dissolution of UO$_2$. *J. Nucl. Mater.* **355**, 38–46 (2006).
34. Clarens, F. et al. The oxidative dissolution of unirradiated UO2 by hydrogen peroxide as a function of pH. *J. Nucl. Mater.* **345**, 225–231 (2005).
35. Odorowski, M. et al. Oxidative dissolution of unirradiated Mimas MOX fuel (U/Pu oxides) in carbonated water under oxic and anoxic conditions. *J. Nucl. Mater.* **468**, 17–25 (2016).

36. Martinez, J. et al. An original precipitation route toward the preparation and the sintering of highly reactive uranium cerium dioxide powders. *J. Nucl. Mater.* **462**, 173–181 (2015).

37. Dacheux, N. & Aupiais, J. Determination of uranium, thorium, plutonium, americium, and curium ultratraces by photon electron rejecting alpha liquid scintillation. *Anal. Chem.* **69**, 2275–2282 (1997).

ACKNOWLEDGEMENTS

AUTHOR CONTRIBUTIONS

T.K.: conceptualisation; data acquisition; data analysis; writing original draft—review—final approval. S.S.: conception of work; data analysis; validation; writing original draft—review—final approval. L.C.: conceptualisation; data analysis; writing—review—final approval. M.C. and R.P.: data acquisition; data analysis; writing original draft—review—final approval. X.L.G. and A.M.: data acquisition; data analysis; writing original draft—final approval. N.D.: conceptualisation; data analysis; validation; writing original draft—review—final approval.

COMPETING INTERESTS

The authors declare no competing interests.

ADDITIONAL INFORMATION

Supplementary information The online version contains supplementary material available at https://doi.org/10.1038/s41529-022-00246-0.

Correspondence and requests for materials should be addressed to Stéphanie Szenknect.

Reprints and permission information is available at http://www.nature.com/reprints

Publisher's note Springer Nature remains neutral with regard to jurisdictional claims in published maps and institutional affiliations.